1-1-2020

Atomically Thin Superconductors

Zhi Li
University of Wollongong, zhili@uow.edu.au

Lina Sang
University of Wollongong, ls906@uowmail.edu.au

Peng Liu
University of Wollongong, pliu@uow.edu.au

Zengji Yue
University of Wollongong, zengji@uow.edu.au

Michael Fuhrer

See next page for additional authors

Atomically Thin Superconductors

Abstract

© 2020 WILEY-VCH Verlag GmbH & Co. KGaA, Weinheim In recent years, atomically thin superconductors, including atomically thin elemental superconductors, single layer FeSe films, and few-layer cuprate superconductors, have been studied extensively. This hot research field is mainly driven by the discovery of significant superconductivity enhancement and high-temperature interface superconductivity in single-layer FeSe films epitaxially grown on SrTiO3 substrates in 2012. This study has attracted tremendous research interest and generated more studies focusing on further enhancing superconductivity and finding the origin of the superconductivity. A few years later, research on atomically thin superconductors has extended to cuprate superconductors, unveiling many intriguing properties that have neither been proposed or observed previously. These new discoveries challenge the current theory regarding the superconducting mechanism of unconventional superconductors and indicate new directions on how to achieve high-transition-temperature superconductors. Herein, this exciting recent progress is briefly discussed, with a focus on the recent progress in identifying new atomically thin superconductors.

Disciplines

Engineering | Physical Sciences and Mathematics

Publication Details

Li, Z., Sang, L., Liu, P., Yue, Z., Fuhrer, M., Xue, Q. & Wang, X. (2020). Atomically Thin Superconductors. Small,

Authors

Zhi Li, Lina Sang, Peng Liu, Zengji Yue, Michael Fuhrer, Qikun Xue, and Xiaolin Wang

Atomically thin superconductors

Zhi Li[1,2†], Lina Sang[1,2], Peng Liu[1,2], Zengji Yue[1,2], Michael Fuhrer[3,4], Qikun Xue[5,6†], and Xiaolin Wang[1,2†]

[1]ARC Centre of Excellence in Future Low-Energy Electronics Technologies (FLEET), University of Wollongong, Wollongong, NSW 2525, Australia

[2]Institute for Superconducting and Electronic Materials (ISEM), Australian Institute for Innovative Materials (AIIM), University of Wollongong, Wollongong, NSW 2525, Australia

[3]School of Physics and Astronomy, Monash University, Victoria 3800, Australia

[4]ARC Centre of Excellence in Future Low-Energy Electronics Technologies (FLEET), Monash University, Victoria 3800, Australia

[5]Collaborative Innovation Center of Quantum Matter, Beijing 100871, China.

[6]State Key Laboratory of Low-Dimensional Quantum Physics, Department of Physics, Tsinghua University, Beijing 100084, China.

Corresponding Author

xiaolin@uow.edu.au; qkxue@tsinghua.edu.cn; zhili@uow.edu.au

Recent years, atomically thin superconductors, including atomically thin elemental superconductor, single layer FeSe film, and few-layer cuprate superconductors, have been studied extensively. The hot research field is mainly driven by the discovery of significant superconductivity enhancement and high-temperature interface superconductivity in single-layer FeSe films epitaxial grown $SrTiO_3$ substrates in 2012. This study has attracted tremendous research interest and generated more studies focusing on further enhancing superconductivity and finding the origin of the superconductivity. A few years later, research on the atomically thin superconductors has extended to cuprate superconductors, unveils many intrigue properties which are never been proposed or observed before. These new discoveries challenge the current theory on the superconducting mechanism of unconventional superconductor and point out new direction on how to achieve high transition temperature superconductors. In this review, we briefly discuss these exciting recent progress. We are aware that there are already some excellent review works on the superconducting mechanism of atomically thin

superconductors. Therefore, this review focuses on the recent progress in identifying new atomically thin superconductors.

1. Introduction

Superconductivity was firstly discovered by Onnes's group in 1911.[1] When measuring the resistivity of Hg at extremely low temperature, they observed a sudden decreasing of resistance to zero at a temperature below 4.2 K. Superconductivity is so fascinating and has attracted enormous studies since the discovery. Now, more than half elemental metals have been confirmed to be superconductors with a transition temperature lower than 10 K. The successful microscopic theory of superconductivity was established in 1957, by Bardeen, Cooper, and Schrieffer (BCS theory).[2] Electron-phonon coupling was identified as the driving force for superconductivity as described by the BCS theory. The isotope effect[3] directly proved the important role of electron-phonon coupling and therefore verified the BCS theory. Then the BCS theory was well-accepted as the standard theory for superconductivity. Superconductors which can be explained by the BCS theory are classified as conventional superconductors.

In 1986, surprising superconductivity of La-based cuprate was discovered with a T_c above 30 K.[4] This discovery immediately induced a fever of searching for High-T_c superconductors from cuprates. Many more cuprates have been found as superconductors and the T_c record of cuprates was pushed to higher than 77 K in one year.[5] In contrast to the rapid progress in discovering new cuprates superconductors, the research on superconductivity mechanism of cuprates is extremely challenging. Many exotic phenomena, including pseudo-gap, d-wave superconductivity, etc., were discovered in cuprates. These interesting phenomena cannot be understood directly from the BCS theory, therefore the cuprates superconductors are classified as unconventional superconductors. In 2007, superconductivity with T_c of 26K was found in iron-based compound LaFeAsO.[6] One year later, T_c was been pushed to a record high of 55

K.[7, 8] The superconductivity of the iron-based compounds also cannot be explained by the BCS theory because of the weak phonon mode. The iron-based superconductors are also been classified as unconventional superconductors and until now, the physical origin of the iron-based superconductivity is still elusive.

The ultimate goal of the research of superconductivity is finding superconductors with a superconducting transition temperature (T_c) at or higher than room temperature. From BCS theory, T_c is limited by the density of states at the Fermi surface and the strength of lattice vibration, which is described by the Debye temperature of phonon. The high density of states at the Fermi surface screens the repulsive Coulomb interaction between electrons. The lattice vibration glues electrons into electron pairs, which are carrying zero resistance current. Materials with rigid lattice, for example, silicon, are generally not good conductors with a large density of states at the Fermi surface. The good conductors, for example, Au and Ag, are lack of strong lattice vibration, and therefore are not superconducting. Therefore, for BCS superconductors, the T_c is limited by the compromise between the density of states and lattice vibration strength.

A clever way to avoid the compromising between the density of states and lattice vibration strength is fabricating interface structures, where one side material with high lattice vibration strength and the other side material with a large density of states. The idea of interface enhancing superconductivity was proposed by Ginzburg in 1964,[9] where excitons instead of phonons are proposed to glue electrons. The superconductor heterostructures including PbTe/PbS, $LaAlO_3/SrTiO_3$, La_2-xSrxCuO$_4$/La_2CuO_4, have been fabricated for the purpose and intensively studied, excellent reviews on these works can be found in references.[10, 11] However, the first significant superconductivity enhancement was observed in single-layer $FeSe/SrTiO_3$ films fabricated by Molecular-beam epitaxy (MBE) method until 2012.[12] Since then, the atomically thin superconductors became a hot research topic and attracted extensive

research studies.[13-15] Most recently, exciting new results were reported on atomically thin cuprate superconductors and proposed a conventional superconductivity scenario for cuprate superconductors. This review will summarize atomically thin superconductor systems, including elemental superconductor, FeSe and cuprate superconductors. This review will demonstrate that the Molecular-beam epitaxy (MBE), scanning tunneling spectroscopy (STM/STS), scanning transmission Electron Microscope (STEM), physical properties measurement system (PPMS), etc., are powerful techniques for fabricating and identifying atomically thin superconductors.

2. Elemental metals grown on semiconductors

Atomically thin metal films grown on semiconductors are usually not considered as favourite superconducting. Because the strong scattering from the interface will destroy long-range orders. Xue's group fabricated high-quality crystalline Pb and In single layers on Si(111) substrates as shown in Figure 1 and conducted systematic scanning tunneling microscopy and scanning tunneling spectroscopy (STM/STS) studies.[16] The high-quality interface prevented the interface scatterings which normally destroy superconductivity. As shown in Figure 2, STS spectra clearly show superconducting gaps. The direct observation of vortex lattice further confirmed the superconductivity. The zero resistivity of In/Si(111) was confirmed by in-situ transport measurements. This proves that superconductivity can survive on single-layer materials.

However, the T_c of single layer Pb and In grown on Si(111) substrates inevitably decreased comparing to their bulk values. The reason is the density states at the Fermi surface are greatly reduced at single-layer thickness. Nevertheless, the interface clearly played an important role in the superconductivity of single layer metals on Si(111) substrates. ARPES data shows a significant enhancement of electron-phonon coupling constant. At the end of the work, the

authors suggest a new route towards atomically thin superconductors: the metal overlay serves as a charge reservoir and the electron-phonon interactions that glue the electrons to form pairs are provided both by the intralayer metallic and more importantly the interface bonds. This prediction has been proved by new atomically thin superconductors discovered in recent years. For example, in 2015, superconductivity with T_c = 5.4 K is discovered on a two-atom layer of hexagonal Ga film grown on semiconducting GaN(0001) by STM and transport measurements.[17]

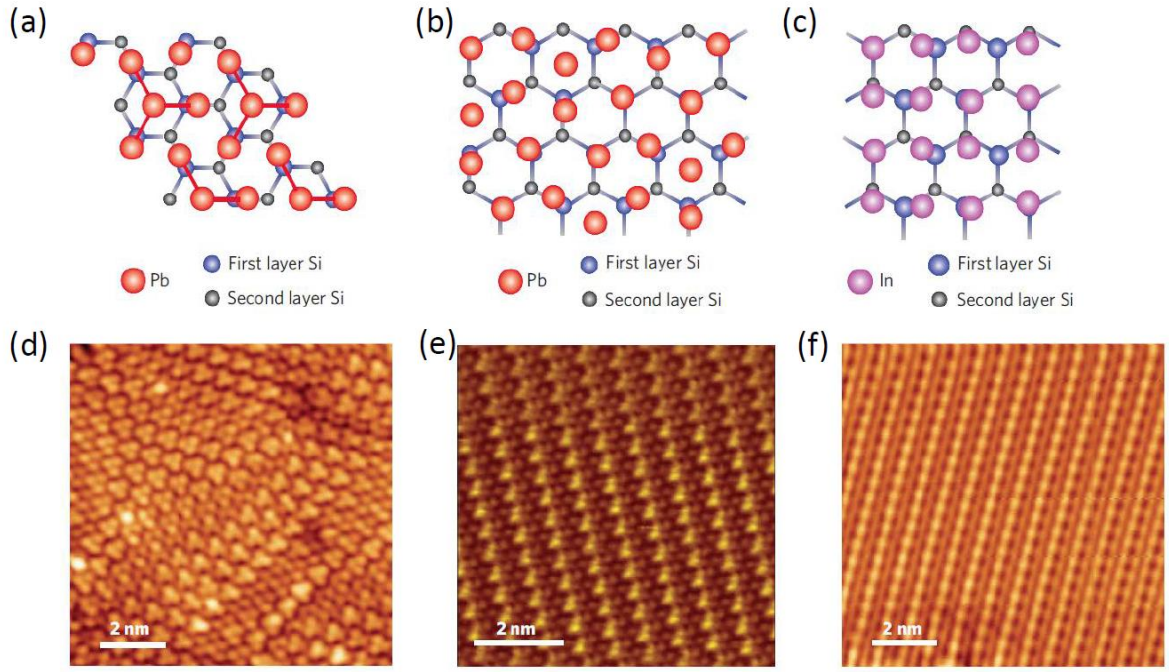

Figure 1. Three types of atomically thin metal films grown on Si substrates. (a-c) and (d-f) are schematic drawings and STM images, respectively. (a) and (d) are SCI Pb/Si(111). (b) and (e) are √7×√3 Pb/Si(111). c and f are √7×√3 In/Si(111).

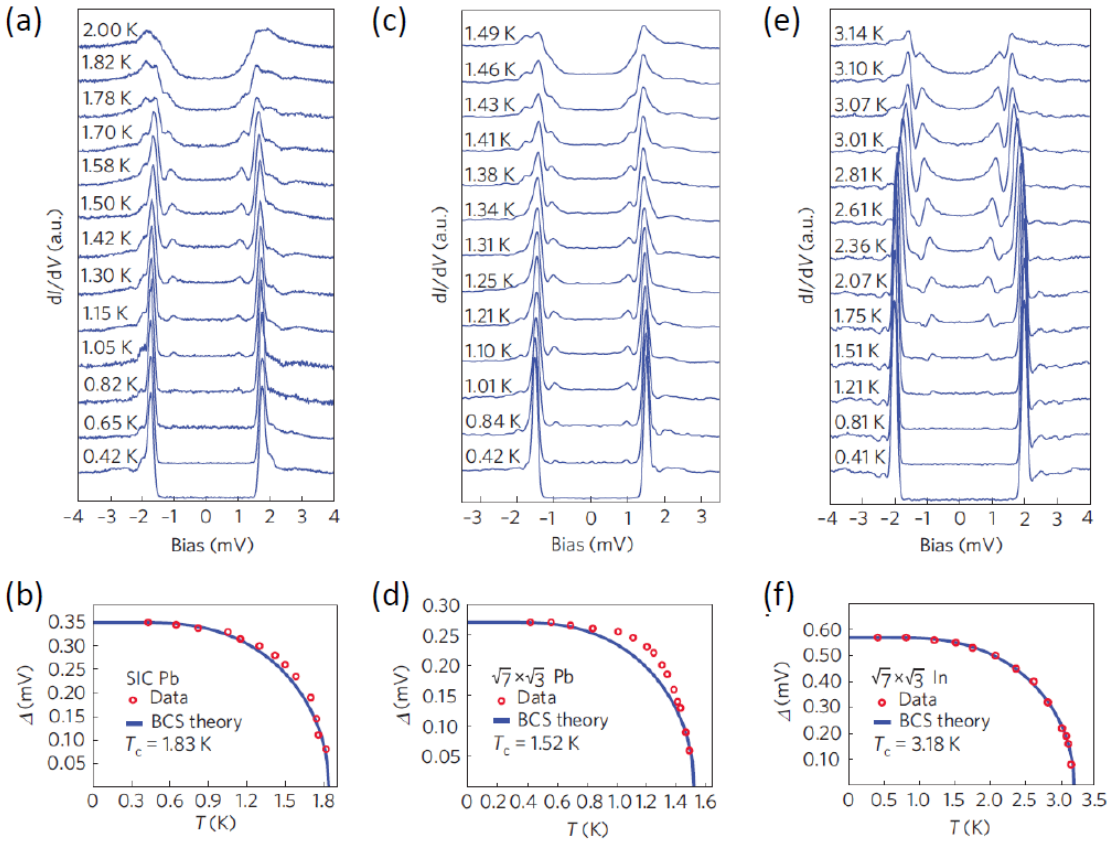

Figure 2. Superconducting gaps characterized by STS spectra (a), SCI Pb/Si(111); (c), √7×√3 Pb/Si(111) and (e), √7×√3 In/Si(111). The corresponding Tc is obtained by fitting with the BCS theory (b), (d), and (f).

3. Single-layer FeSe superconductors on various insulating substrates

3.1 Structure and superconductivity of bulk FeSe

FeSe only contains two elements and has the simplest structure in iron-based superconductor family. FeSe has several phases, where only the PbO-structure tetragonal phase β-FeSe is superconducting with a T_c ~ 8 K.[18] In this review, we only discuss the β-FeSe and refer it as FeSe for concise. As shown in Figure 3, FeSe is a layered compound. In each layer, Fe atoms are sandwiched between the top and bottom Se atoms. The layers are weakly coupled by van der Waals interaction. The in-plane lattice constant (*a* and *b* direction) is 3.78 Å and the lattice constant along the c direction is 5.50 Å.

The superconductivity of bulk FeSe has been extensively investigated because of its simplicity in structure and attractive properties. The T_c of bulk FeSe can be pushed to 37 K at a high pressure of 8.9 GP.[18, 19]

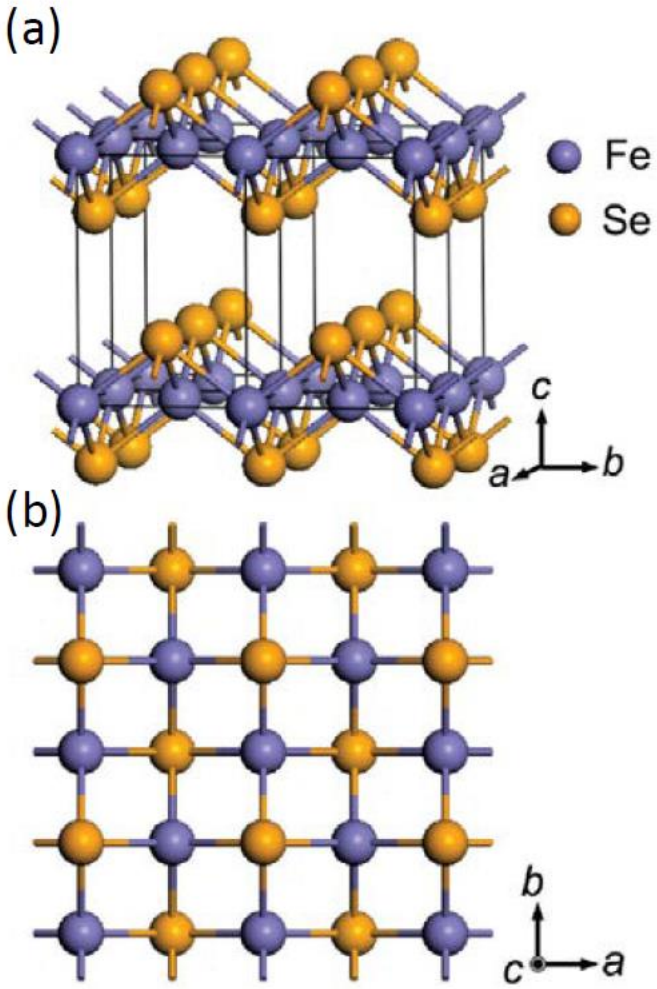

Figure 3. Schematic drawing of β-FeSe lattice structure. (a) 3D model. (b) Top view.

3.2 Few layer FeSe films grown on graphene substrates by MBE method

High quality stoichiometric FeSe films with varies thickness was fabricated on graphene substrates by MBE method and studied by in-situ STM.[20] By keeping a Se-rich condition, where the Se flux is approximately 10 times of Fe flux, the stoichiometry of FeSe is

automatically achieved. This is a well-established epitaxial method for layered semiconductors, e.g. GaAs. The as-grown FeSe films show a √5×√5 phase with excess Se, which is non-superconducting.[21] The superconducting phase can be obtained by post-annealing at a higher temperature, which eliminates the excess Se atoms. Since graphene is a chemically inert material, the superconducting properties of FeSe films grown on graphene substrates are not modulated by the graphene substrates. Measuring from the atomic resolution STM images, the lattice structure superconducting transition temperature is almost identical with bulk FeSe crystals. Remarkably, a few-layer FeSe flake can glade and rotate on the graphene substrate.[21]

The high-quality FeSe films lead to discovering of more intrinsic properties, including the V-shape superconducting gap and C2 symmetry, helping the understanding of the superconductivity pairing mechanism of iron-based superconductors. One interesting observation is that the T_c of FeSe films shows a linear relation with the inverse of film thickness. The single-layer FeSe/graphene is not superconducting at a temperature above 2 K. The decreasing of T_c with decreasing of films thickness is common in conventional BCS superconductors, because of decreasing of DOS at the Fermi surface for thin films. However, FeSe is generally believed to be an unconventional superconductor. The success of MBE grown high-quality FeSe films provided a new platform for investigating iron-based superconductor.

3.3 single-layer FeSe films on $SrTiO_3$ substrates

Because of the inertness of graphene substrates, no interface superconductivity enhancement effect is observed on FeSe films grown on graphene substrates. To increase T_c of FeSe films by interface effect, a strong interaction between FeSe films and substrates should be introduced. However, this is more challenging for MBE growth. Since the in-plane lattice constant of STO(100) is comparable to the in-plane lattice constant of FeSe. In 2010, Xue's group started to growth FeSe films STO(100) substrates. Unlike graphene, as-purchased STO substrates have

varies of surface reconstructions. Direct grown FeSe films on as-purchased STO substrates usually consist of a wetting layer. FeSe films will growth on the wetting layer. Therefore, high quality atomically thin FeSe films cannot be obtained by deposition FeSe on as-purchased STO substrates. To get a high-quality interface, before growing FeSe films, STO substrates are annealed to a high temperature (950 °C) under Se flux to get rid of contaminations and get a uniform clean surface. Similar to the growth of FeSe films on graphene, the epitaxy growth of single-layer FeSe films on STO substrates also requires a Se-rich condition and post-annealing to achieve superconducting.

The superconducting single-layer FeSe/STO films are investigated by STM/STS and transport measurements (Figure 4).[12] Detailed STM and STS studies are conducted on single-layer FeSe films grown on Nb-doped STO substrates. The striking observation is a significant large U-shape superconducting gap Δ=20.1 meV, which is 9.1 times of the gap (Δ~2.2 meV) of bulk FeSe, where the Tc of bulk FeSe is 9.4 K. Optimistically, we can expect a high Tc even exceeding 77 K if the superconducting mechanism of the single-layer FeSe/STO is the same with the bulk FeSe. The superconductivity of single-layer FeSe/STO is further confirmed by the observation of vortex when applied a perpendicular magnetic field. Transport measurements are conducted on single-layer FeSe films grown on insulating STO substrates to determine the Tc. However, this work is very challenging experimentally. The first reason is that insulating STO substrates become very conductive after annealing at 950 °C due to creation of a large number of oxygen vacancies, which makes it is almost impossible to measure the small conductance contribution from the single FeSe layer. Therefore, this efficient method of obtaining high-quality STO surface cannot be applied to insulating STO substrates. Another reason is that single-layer FeSe films are fragile in the air, extra protection layers are necessary for ex-situ transport measurements. Up to now, the best protection layer for single-layer FeSe is FeTe films.[22] Nevertheless, the protection layers inevitably introduced unwanted

perturbation to the superconductivity of single-layer FeSe/STO and led to a lower T_c from transport measurements. Because of these reasons, T_c determined by ex-situ transport measurements varies in a large range, and the highest Tc reported by ex-situ measurement is above 80 K.[22-25] It is worth to note that the in-situ transport measurement suggests a resistance jumping to zero at a temperature higher than 100 K,[26] which is to be supported by in-situ diamagnetic measurements to confirm a superconducting transition. Another striking observation is that only first layer FeSe, which is directly bonded with STO substrates, is superconducting. The second layer and thicker FeSe layers are not superconducting. Therefore, it is obviously that interface played an important role in the high temperature atomically thin FeSe superconductor. To deeper explore the enhanced T_c in monolayer FeSe films, various interface effects, like charge transfer, the interfacial electron-phonon coupling, the tensile strain effect, and the screening effect are all proposed and studies extensively.[27-33] Heavy electron doping and strong eletron-phonon coupling are identified on single layer FeSe films growth on STO substrates.

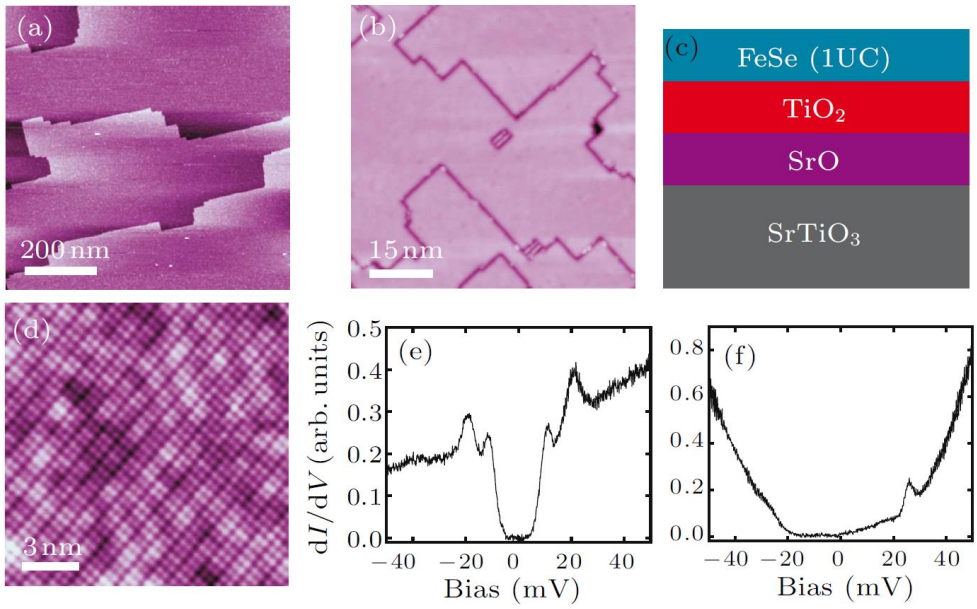

Figure 4. Superconductivity in single-layer FeSe films grown on STO substrates. (a) Typical STM image of STO(001) substrate. (b) STM image of the 1-UC-thick FeSe film on STO(001).

(c) Schematic drawing of FeSe/STO superconducting film. The TiO_2 layer is believed played an important role in the superconductivity. (d) Atomically resolved STM image of single-layer FeSe/STO film. (e) STS on single-layer FeSe film showing superconducting gap with pronounced coherence peaks appear at ±20.1mV and ±9mV, respectively. (f) STS on second layer FeSe showing semiconductor-like (non-superconductive) behaviour.

3.4 single-layer FeSe films on anatase TiO_2 substrates

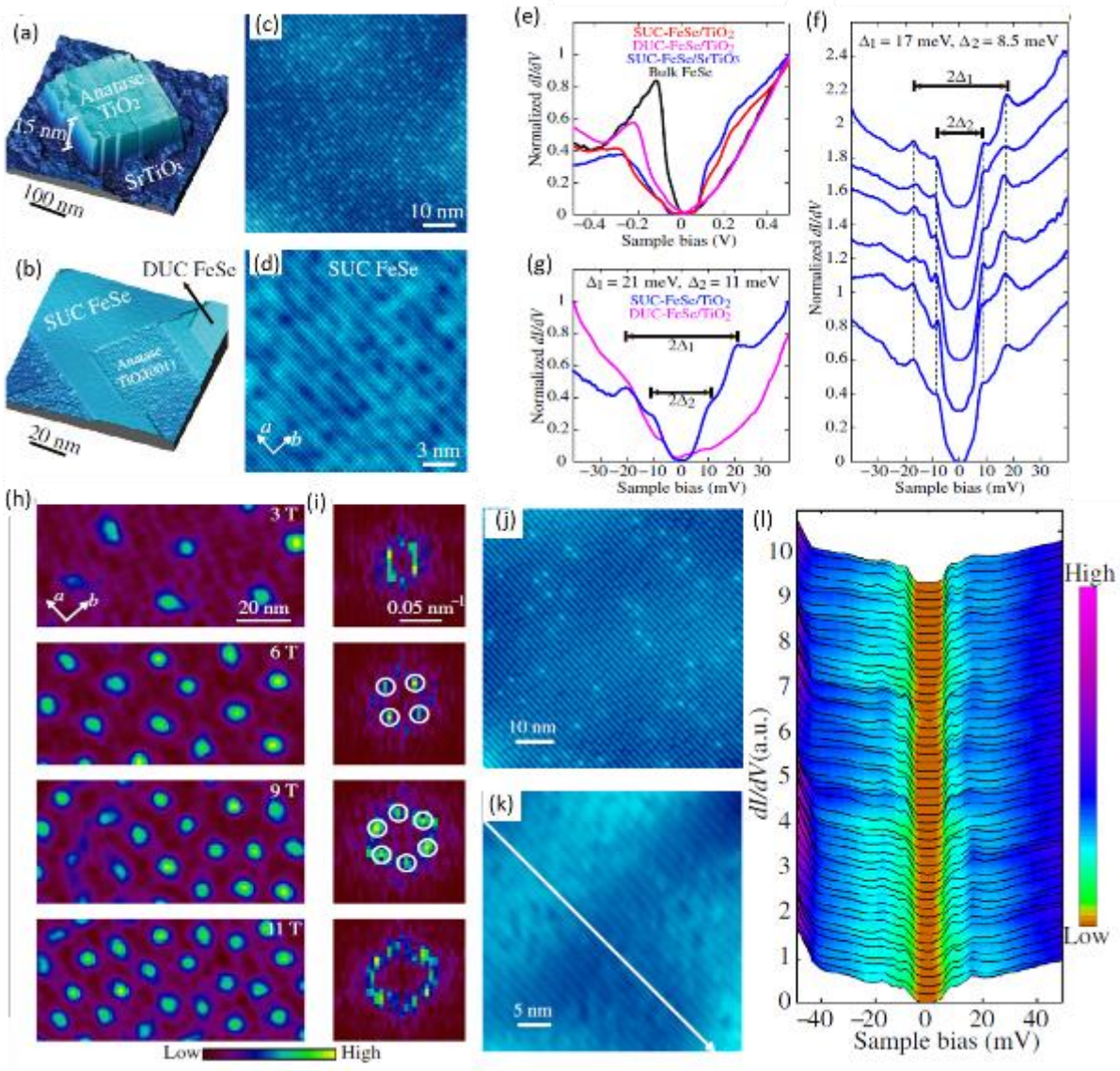

Figure 5. (a) STM topography showing an anatase TiO_2 (001) island with a thickness of 15 nm on $SrTiO_3$(001) substrate. (b) SUC and DUC FeSe films on anatase TiO_2. (c) Enlarged STM

topography acquired on a TiO_2 island. (d) Atomically resolved STM topography of SUC FeSe film. (e) large-energy-scale dI/dV spectra for FeSe films on anatase TiO_2(001) (red and magenta curves) and $SrTiO_3$ (001) (blue curve), and bulk FeSe (black curve). (f), (g) Low energy dI/dV spectra for various SUC FeSe films on TiO_2 (001) (blue curves) and DUC FeSe films on TiO_2 (001) (magenta curves). (h) zero-bias-conductance (ZBC) map showing the vortices under various magnetic fields in SUC FeSe/TiO_2 (001). (i) FFT power spectra of the ZBC maps in (h). (j) STM topography for annealed anatase TiO_2 (001). (k) Atomically resolved STM topography of SUC FeSe/annealed anatase TiO_2 (001). (l) A series of dI/dV spectra acquired along the white arrow in (k) for every nanometer, revealing the almost identical superconducting gap magnitude (~17 meV).[34]

In order to clarify if the $SrTiO_3$ impose additional effect(s) other than electron doping to increase the T_c. The anatase TiO_2 (001) substrate is studied by STM and compared with the STO. The results show that the high T_c superconductivity and magnetic vortices in single-unit-cell (SUC) FeSe/anatase TiO_2 (001) was obtained.[34]

For anatase TiO_2(001), the in-plane lattice constant ~0.3782 nm is larger than $SrTiO_3$ (001)~ 0.3905 nm but very similar to FeSe~0.3765 nm. Figure 5b shows STM topography for the single-unit-cell (SUC) and double-unit-cell (DUC) FeSe films on anatase TiO_2(001). The STM measurements show that both SUC and DUC FeSe/anatase TiO_2 have the same in-plane lattice constant~0.380±0.005 nm, reflecting the absence of strain force formation in the FeSe/anatase TiO_2.[20, 35]

Figure 5e displays the dI/dV spectra in a large-energy-scale for SUC-FeSe and DUC-FeSe films on anatase TiO_2 and SUC-FeSe/STO, and the bulk FeSe. The measurements show the overall feature for SUC-FeSe/anatase TiO_2 is similar to SUC-FeSe/$SrTiO_3$ and K-doped FeSe films, different from the bulk FeSe and DUC-FeSe/anatase TiO_2, which suggesting the

interface charge transfer from the anatase TiO_2 substrate to the SUC FeSe films. Low energy dI/dV spectra for various SUC FeSe films on anatase TiO_2 give the evidence of superconductivity, as shown in Figure 5f and 5g. The result reveals that the double gap Δ1 and Δ2 are 17 and 8.5 meV, respectively (Figure 5f). In addition, the DUC FeSe/anatase TiO_2 show absence of superconductivity features due to the lack of sufficient interface electron transfer from anatase TiO_2 substrate to DUC FeSe films. To further verify the opening gap is related to superconductivity, a high magnetic field is applied, an Abrikosov vortices lattice is formed, as shown in Figure 5 h, i.

In addition, anatase TiO_2 has a unique feature of oxygen vacancies, which is easily tuned in their density by annealing and visualized by STM.[36] The oxygen vacancies in the superconductivity of SUC FeSe can be directly identified by STM. As shown in Figure 5c, j, the oxygen vacancy density is about 4.6×10^{-2} and 6.1×10^{-3} per nm^2 for anatase $TiO_2/SrTiO_3$ and annealed anatase $TiO_2/SrTiO_3$, respectively, showing a significantly reduced surface oxygen vacancy density. By STM measurements, the superconducting gap and FeSe morphology are almost unchanged, as shown in Figure 5k. Thus, the surface oxygen vacancies are excluded for charge transfer.

3.5 Single-layer FeSe films on MgO substrates

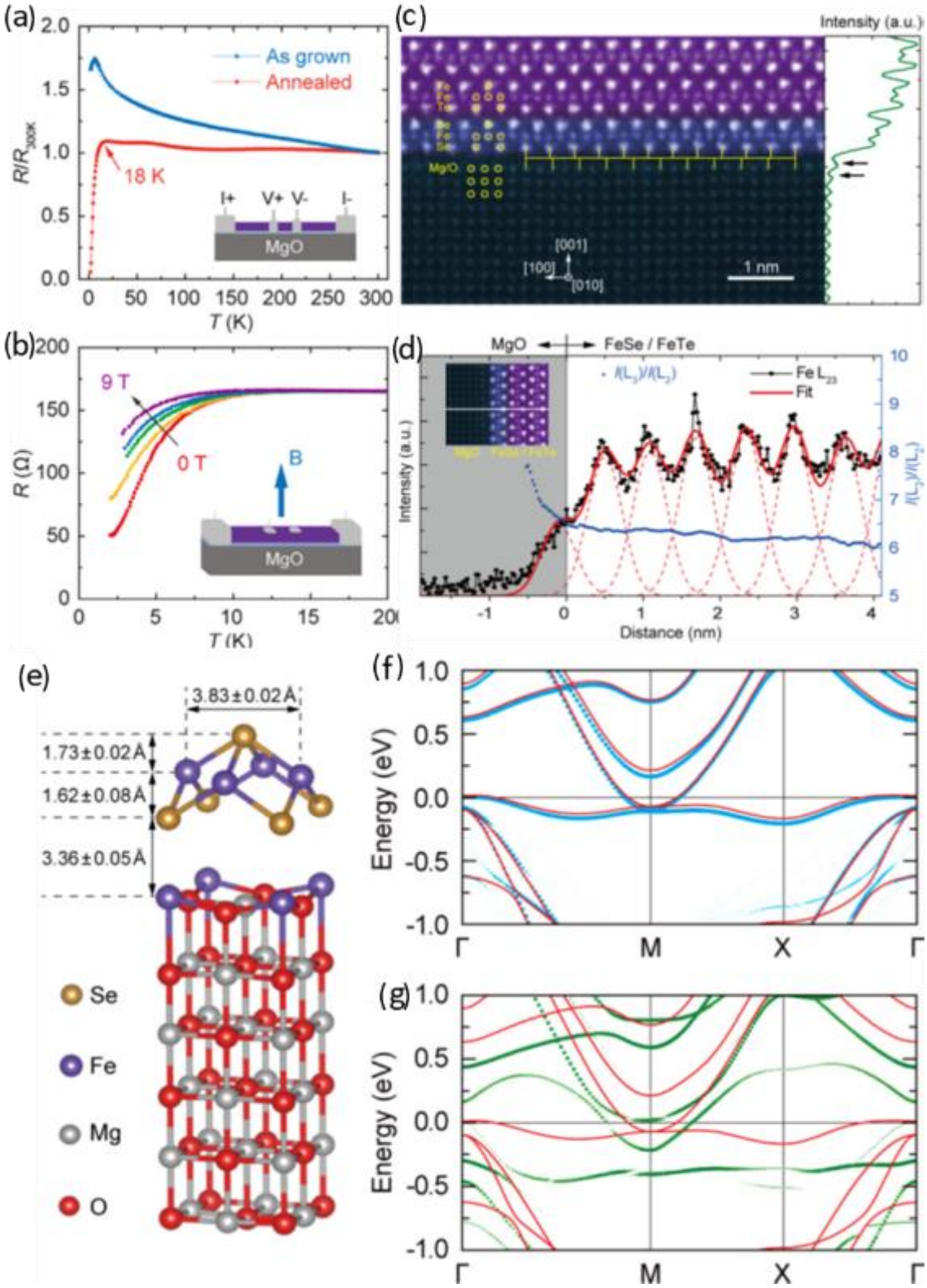

Figure 6. (a) The temperature dependence of resistances normalized to the values at 300 K for both as-grown and annealed monolayer FeSe samples. (b) The temperature dependence of resistances for another annealed sample under external out-of-plane magnetic fields up to 9 T.

(c) STEM and (d) EELS characterization of FeTe/FeSe/MgO(001) heterostructures. (e) Schematic structure of monolayer FeSe on MgO(001) with 50% Fe substitution in the topmost MgO layer. (f) DFT calculated band structure of monolayer FeSe on pristine MgO(001) (blue dots) and (g) on Fe-substituted MgO(001) (green dots), in comparison with freestanding monolayer FeSe (red dots).

Single-layer FeSe films have been prepared on another oxide MgO(001) substrates. The study shows that the atomic substitution can cause charge transfer and thus the high T_c superconductivity in monolayer FeSe films, the Fe atoms diffuse into the MgO layer at the interface and substitute Mg atoms, induce the charge transfer from the MgO substrate to the FeSe films. For the monolayer FeSe films on the MgO substrate, the $T_{c,onset}$ is about 18 K, higher than the T_c~8K for the bulk FeSe.[18, 37]

Figure 6a shows the resistance increases with the decreasing of temperature until down to 6K for the as-grown monolayer FeSe, which is mainly due to interface effect induced the stoichiometry change in FeSe film with Se-rich.[27, 38] For the annealed FeSe films, the $T_{c,onset}$~ 18 K is observed. In Figure 6c, the topmost two Mg layers look brighter intensity contrast to the bulk Mg atoms, marked by black arrows, indicating therein other heavier atoms, such as Fe. Figure 6d show electron energy loss spectroscopy (EELS) characterization of FeTe/FeSe/MgO(001) heterostructures. The peak just appears at the location of Fe layers for the monolayer FeSe and cap layer FeTe, but it is worth noting that there is an extra peak on the MgO side at the interface, which further show the Fe atoms diffuse into the top MgO layers. For the topmost two MgO layers, the periodic structure did not change and no other additional features occurred. So, the diffused Fe atoms in MgO layers is mainly a substitute for Mg atom.[39]

Density functional theory calculate the band structure of monolayer FeSe on pristine MgO(001), monolayer FeSe on 50% Fe substituted MgO(001), and the freestanding monolayer FeSe, which are represented by blue dots, green dots, and red dots respectively. Compare with the energy bands of freestanding monolayer FeSe, it moves slightly downward for FeSe/pristine-MgO, indicating there is a small amount of electron doping in monolayer FeSe films, as shown in Figure 6f. The energy bands move remark downward for FeSe/Fe-substituted-MgO, indicating there are substantial electron doping in the monolayer FeSe films, as shown in Figure 6g. In the monolayer FeSe, the topmost MgO and the second MgO layers, the numbers of electrons for each Fe atom are 7.4, 6.9, and 6.6, via DFT calculations, indicating the diffused Fe atoms in MgO layers lose electrons. Thus, the above calculations reveal that the atoms substitution at the interface promotes the interface charge transfer from the Fe-substituted MgO substrate to the FeSe films, lead to the T_c enhancement.

4. Atomically thin cuprate superconductors

Perovskite-type cuprates have the highest transition temperature (>130 K) in the family of superconductors, much higher than the boiling point (77 K) of liquid nitrogen. In their layered crystal structure, the CuO_2 planes are situated between other metal-oxide layers that act as charge reservoirs to induce superconductivity in CuO_2.[40-43] Superconducting cuprates are classified into unconventional superconductors, for the reason that their high transition temperatures are hard to be understood with conventional BCS theory. The real mechanism of high-temperature superconductivity in cuprates is still the biggest challenge for condensed matter physics. Therefore, extensive experimental and theoretical research has been dedicated to exploring new phenomena and their interaction with superconductivity.[44-48] In this section, we summarize recent key findings on ultrathin superconducting cuprates.

$Bi_2Sr_2CaCu_2O_{8+\delta}$ (Bi2212) is the most widely studied compound among cuprate superconductors. Within Bi2212, superconducting CuO_2 bilayers are stacked alternately with

BiO/SrO building blocks along the c-axis. Bi2201 and Bi2223 are another two derivatives of Bi2212, depending on the number of CuO_2 planes in one unit cell. Bi2201, Bi2212, and Bi2223 exhibit superconducting phase transitions at 34, 90, and 110 K, respectively.[49] The first two-dimensional (2D) superconductor was produced by exfoliating a Bi2212 crystal down to monolayer.[50] Atomically flat Bi2212 with clean surfaces can be readily obtained by cleaving Bi2212 crystals along BiO planes, as a result, that the bonding between them is van der Waals force.[51] Most of the current surface-sensitive characterizations are carried out on the BiO surface planes of exfoliated Bi2212 thin flakes.[51-53] The CuO_2 plane, ≈ 5 Å underneath the BiO surface, is blocked from a STM tip by upper BiO and SrO layers.[53] Typical features of BiO surface seen by STM are nearly commensurate crystal supermodulation and concomitant dark-atom rows along supermodulation corrugation.

Besides the BiO plane, it is highly desired to directly examine the role of each oxide layer in Bi2212. A state-of-the-art argon-ion bombardment and annealing (IBA) technique were employed to precisely expose each plane of Bi2212, including BiO, SrO, and CuO_2.[54] The whole process was conducted in a Unisoku ultrahigh vacuum (UHV) low-temperature STM system equipped with an ozone-assisted molecular beam epitaxy (MBE) chamber and supporting components of IBA. Under UHV, an in-situ cleaved Bi2212 was annealed at 450 °C for getting an optimal superconducting temperature (91 K), which was further processed by argon-ion bombardment in a low-pressure argon atmosphere to expose other planes. The Bi2212 flake processed by IBA shows highly clean and atomically flat surface where different exposed planes from terrace morphology with various heights, Figure 7a. Seven planes are identified in Figure 7b by matching with crystal planes along the *c* axis, including four BiO, two CuO_2, and one SrO layer. The electronic structure of each layer (Figure 7i-k) was characterized by STM at 4.2 K. The BiO(I) plane exhibits V-shaped density of states (DOS) at the Fermi level (E_F), indicating inherent pseudo-gap in BiO. The metallic nature of the SrO

plane is reflected by a distinct peak at E_F peak that is a symbol of van Hove singularity (VHS). However, the VHS only emerge in SrO plane when parent Bi2212 shows recovered superconductivity via IBA treatment. Two-energy-scale gaps are observed for CuO_2(I) and CuO_2(II). Remarkably, the smaller-energy-scale gaps (Δ) of CuO_2 become invisible at 78 K (Figure d) quite closed to T_c, revealing that the Δ gap is the only superconducting gap for CuO_2. In addition, the energy gap of CuO_2(I) is larger than that of CuO_2(II), as a result, that the adjacent SrO layer dopes more holes into CuO_2(II) as carrier reservoir. Therefore, the CuO_2/SrO bilayer could be crucial sources for high-temperature superconductivity of Bi2212.

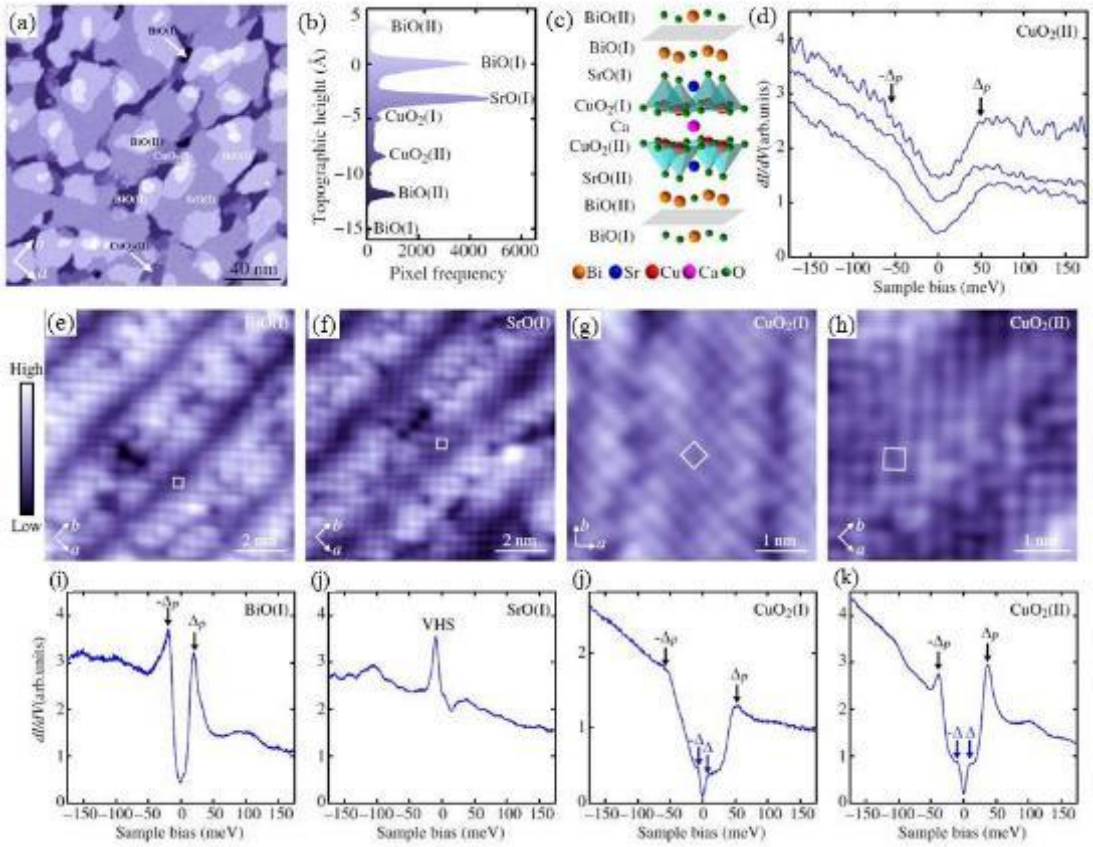

Figure 7. (a) STM topographic image of the Bi2212 thin flake prepared by IBA technique, demonstrating terrace morphology on the surface. (b) The relationship of the frequency with the topographic height of various planes. (c) Schematic crystal structure of Bi2212, in which different metal-oxide layers are stacked alternately along the c-axis. The grey sheets represent

the easily cleaved planes of Bi2212 crystals. (d) Electronic spectra of CuO_2 (II) at 78 K. (e-h) STM topographies and (i-k) electronic spectra on various planes of BiO(I), SrO, CuO_2 (I), and CuO_2 (II) of Bi2212 measured at 4.2 K, respectively. White squares mark the in-plane unit cell of each plane, with a periodicity of 3.8 Å.[54]

The IBA technique was also employed to process the $Bi_2Sr_2CuO_{6+\delta}$ (Bi2201) superconductor. A comparative study between Bi2201 and Bi2212 was made with regard to electronic structures. Pb-doped Bi2201 single crystals in the extremely overdoped region (T_c = 4 K) were selected for investigating features of Bi2201. Four planes of BiO(I), SrO(I), BiO(II), and BiO(I′) were identified from STM topography (Figure **8**8b). The absence of CuO_2 planes might be attributed to the fact that CuO_2 in Bi2201 is strongly bonded with a pair of SrO layers, by contrast, that CuO_2 is coupled with only one SrO layer in Bi2212. When treated with various post-annealing conditions, the BiO planes exhibit either VHS or pseudogap around E_F. The magnitude of pseudogap with coherence peaks is anomalously large up to 49 meV. The existence of VHS as charge carrier reservoir in the as-cleaved BiO(I) plane is favored by adequate interstitial oxygen dopants, which can be quickly converted into pseudogap by UHV annealing for just 10 min (Figure **8**8d). Noticeably, the only pseudogap is observed in the SrO planes (Figure **8**8e). It is in marked contrast to Bi2212 in which VHS solely appears on the SrO plane. Opposite structural buckling in Bi2201 and Bi-2212 is responsible for their contradictory VHS distribution. As shown in Figure **8**8c and 8f, the structural bucking is stronger for BiO in Bi2201 and for SrO in Bi2212, respectively. Furthermore, the doping efficiency of charge carriers in BiO planes into CuO_2 planes is largely lower than that in SrO planes, due to the far distance between BiO and CuO_2. These findings are solid evidence to explain why the superconducting T_c of Bi2212 is far higher than Bi2201.

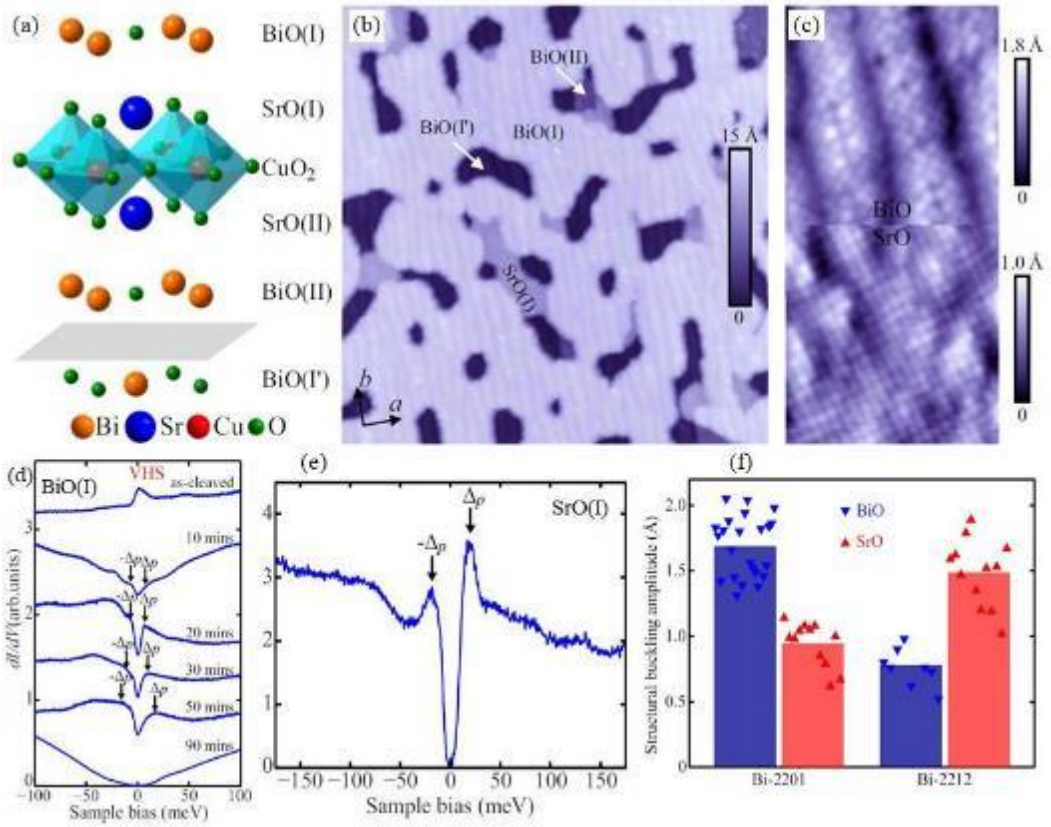

Figure 8. (a) Schematic crystal structure of Bi2201, where CuO_6 octahedra are sandwiched by BiO/SrO building blocks. The grey sheets represent the easily cleaved planes of Bi2201 crystals. (b) STM topography of the Bi2201 crystal treated by IBA technique. Four planes of BiO(I), SrO(I), BiO(II), and BiO(I′) are identified on the terrace-like surface. (c) STM topographies showing the structural buckling of the BiO and SrO planes in Bi2201. (d) Evolution of dI/dV spectra of the as-cleaved BiO(I) plane with prolonged UHV reduction annealing at 500 °C. (e) dI/dV spectra on the SrO(I) planes treated with zone exposure of 18 000 Langmuir. (f) Amplitudes of structural buckling on the BiO and SrO planes of Bi2201 and Bi2212. Each triangle is the measured amplitude from a STM topography, while colored bars are averaged amplitudes.

It is noticeable that the exposed CuO_2 planes by argon-ion bombardment are not large enough to characterize adequate properties associated with superconductivity. A novel design was proposed to fabricate large-scale CuO_2 monolayer on the BiO surface of the cleaved

$Bi_2Sr_2CaCu_2O_{8+\delta}$ (Bi2212) by ozone MBE method, which opens a new path to directly explore superconducting CuO_2.[55] Typically, CuO_2 films were deposited onto the Bi2212 surface by evaporating copper sources under ozone flux beam in ultrahigh vacuum. Atomically flat CuO_2 layer without defects can be easily found in areas of 40 nm x 40 nm, Figure9a-b. The electronic structure of CuO_2 monolayer with the T_c of 91 K was directly measured by in-situ scanning tunneling microscopy. There were two-energy-scale quasiparticle gaps separately distributed in different regions of the CuO_2 layer, as shown in Figure9c-e. At the boundary area, a double-gap feature was observed as the mixture of two types of gaps. The V-like gap was identical to pseudo-gap from the cleaved BiO surface. The U-like gap showing strong phase coherence originates from a nodeless s-wave superconducting gap in CuO_2 layer. This finding is in marked contrast to the well-known nodal d-wave pairing symmetry for high-T_c cuprate superconductors. When K, Cs, and Ag atoms are absorbed on the CuO_2 film, U-like gap keeps undisturbed against scattering by these non-magnetic impurities. A charge-transfer mechanism is responsible for the nodeless superconductivity of CuO_2 monolayer on Bi2212 substrate, in which two-dimensional hole liquid is formed in the CuO_2 layers and the Bi2212 substrate serves as a charge reservoir.

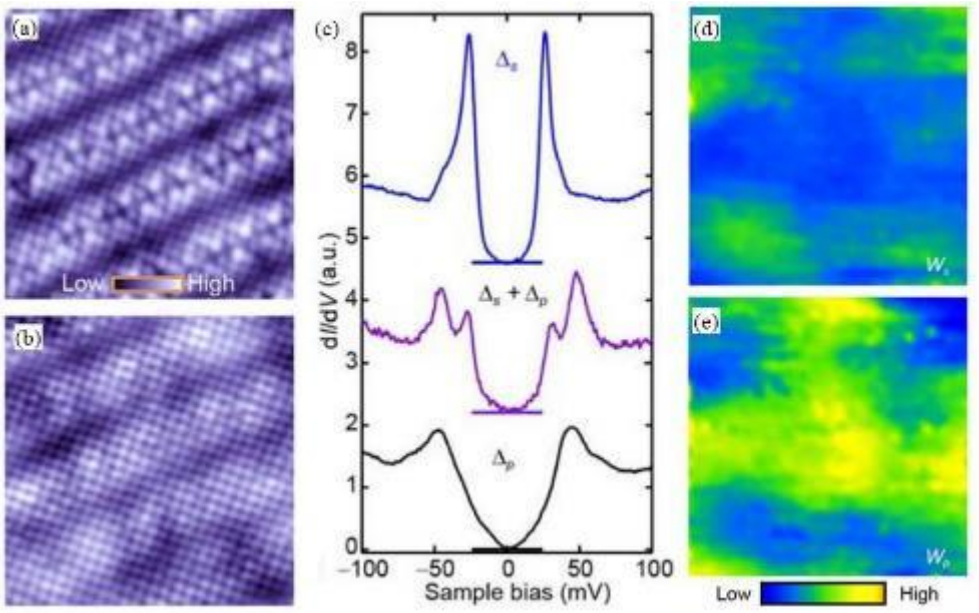

Figure 9. STM topography (10 nm x 10 nm) of (a) the BiO surface layer and (b) the CuO_2 film; (c) dI/dV spectra of the CuO_2 films. The U-like gap (Δs) and V-like (Δp) gap in the low-energy quasiparticle excitations were observed in different regions. The double-gap feature (purple) appears at the boundaries, showing mixed U- and V- gaps. Horizontal lines in various color represent zero-conductance positions; Local DOS images from the mapping of dI/dV conductance at energies of (d) superconducting gap Δs and (e) pseudogap Δp, directly displaying the spatial distribution of spectral weight $W_{s(p)}$.[55]

Various theoretical scenarios have been proposed to further understand the superconductivity in the CuO_2 monolayer grown on a Bi2212 substrate. Jiang *et al.* proposed that CuO_2 monolayer possesses a new electronic structure related to interface charge transfer so that CuO_2 monolayer is heavily overdoped into the hole-rich regime.[56] Cu $d_{x^2-y^2}$ and $d_{3z^2-r^2}$ orbitals are important components of the electronic structure. Different from bulk cuprates, CuO_2 monolayer nodeless inherently owns s-wave superconducting state that is generated by spin-orbital exchange interactions. This scenario fitting experimental observations also points the way of developing new high-T_c superconductors in ozone grown transition-metal-oxide monolayer heterostructures. Zhu *et al.* argued that CuO_2 monolayer exhibits proximity-induced superconductivity from the Bi2212 substrate.[57] The U-like superconducting gap well suits a two-orbital model of the hybridized oxygen p_x and p_y orbitals, and possibly results from a mixture of d-wave and s-wave pairing. The nodeless gap in the two-orbital model could appear if the on-site pairing coupling is as strong as the energy splitting in the two bands.

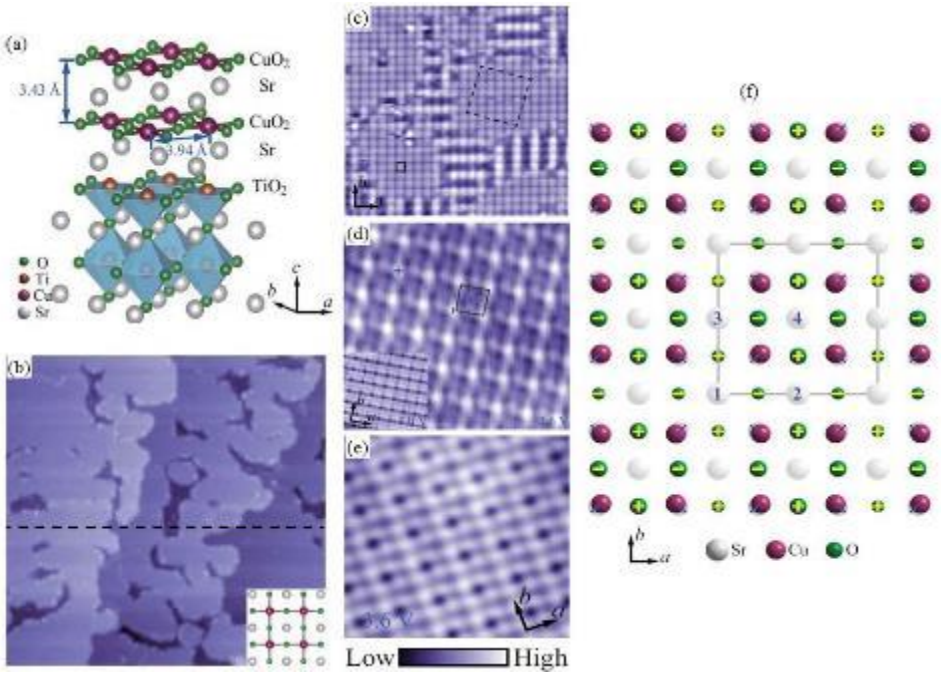

Figure 10. (a) Schematic structure of Infinite-layer $SrCuO_2$ film formed on TiO_2-terminated $SrTiO_3$ (001) substrate. (b) STM topography of layer-by-layer $SrCuO_2$ thin film with a thickness of 6 unit cells. Inset is the top view of $SrCuO_2$ with four CuO_2 plaquettes. (c) High-resolution STM topography revealing a 2×2 checkerboard square lattice of surface CuO_2 plane. (d) STM image of subsurface Sr atoms with a sample bias of −3.6V, only Sr1 and Sr2 atoms are visible. Inset shows the STM image of surface CuO_2 in the same area with a larger bias of −4.0V. (e) Atomic resolution images of CuO_2 plane with a sample bias of −3.6V. (f) Up-down oxygen buckling model. The plus (+) and minus (−) signs demonstrate the oxygen ions displacing upward and downward with regard to the CuO_2 plane, respectively. The size of the green spheres represents the buckling strength. The shaded plum spheres show the shifting of the Cu atoms.[58]

Infinite-layer (IL) $ACuO_2$ (A = Ca, Sr, Ba) compounds are another series of high-T_c superconductors among cuprates. They typically have no apical oxygen and prefer terminating with the CuO_2 layer. It is favorable to directly examine the feature and properties of the CuO_2

plane in IL cuprates, exploring the mystery of high-temperature superconductivity. Ultra-thin epitaxial films of the $SrCuO_2$ IL compound were grown on $SrTiO_3$ substrates by MBE in a layer-by-layer manner, whose atomic-scale structure was systematically studied with in-situ STM.[58] A key preparation step is to generate TiO_2-terminated $SrTiO_3$ by annealing at 1200 °C before thin film deposition. The schematic diagram of $SrCuO_2$ films on TiO_2-terminated $SrTiO_3$ is shown in Figure 10a. The thickness of a typical layer of $SrCuO_2$ is about 3.5 Å. STM topography (Figure 10c) demonstrates checker-board-like square lattice with a spacing of ~7.9Å, validating the surface of $SrCuO_2$ film is actually stoichiometric CuO_2 with 2×2 reconstruction. Such reconstruction is ascribed to preferential structural distortions of four adjacent CuO_2 plaquettes. Only half subsurface Sr atoms are visible for STM (Figure 10d), indicating intra-cell rotational symmetry breaking. A periodic up-down buckling model (Figure 10f) of oxygen ions on the CuO_2 plane was proposed as for the observed surface reconstruction and symmetry breaking.

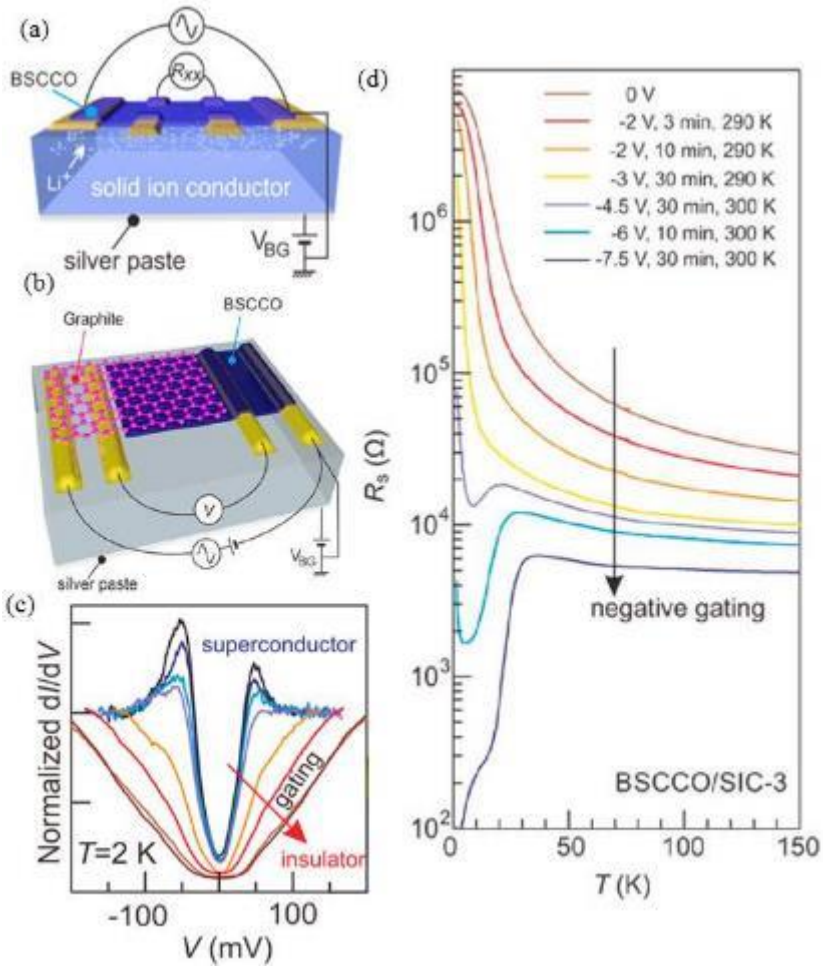

Figure 11. Schematic diagram of (a) solid-state gating configuration and (b) Graphene/BSCCO heterostructure designed for measuring tunneling spectroscopy. (c) Tunneling dI/dV spectra of G/BSCCO/SIC collected at various gating conditions. Dashed lines mark gap magnitudes Δ±. (d) The sheet resistance of a BSCCO flake on SIC with negative gating voltages inducing lithium ions deintercalation.[59]

Tuning charge carrier density by field-effect gating has been an efficient approach to manipulate correlated phases of cuprate superconductors and to investigate their connections with superconductivity. Gate-induced superconductor-insulator transition (SIT) was achieved in ultrathin $Bi_2Sr_2CaCu_2O_{8+\delta}$ (BSCCO) flakes with using solid ion conductor (SIC) as electrolytes.[59] In addition, combing ionic gating with tunneling spectroscopy allows achieving complex quantum phase diagram of BSCCO with a single sample. The BSCCO flake

with a thickness of 39 nm was stamped onto the pre-patterned SIC substrate by dry transfer technique, Figure 11a. When changing back-gate voltages (V_{BG}), electric fields induce lithium-ion intercalation and deintercalation within the BSCCO lattice, causing modulation of charge carrier density. As the positive V_{BG} increases, BSCCO shows a drop of superconducting temperature (T_c) from the original 50 K and finally turn into an insulating regime. Scaling analysis proved this SIT in Bi-2212 is a two-dimensional quantum phase transition (2D-QPT). Furthermore, tunneling spectroscopy in graphite(G)/BSCCO heterojunctions was conducted to understand the evolution of the density of states across the SIT. V-shaped gaps are observed in the critical regime of the SIT, where superconductivity starts to fully vanish. When BSCCO turns more insulating, the density of states is further suppressed in a symmetric manner.

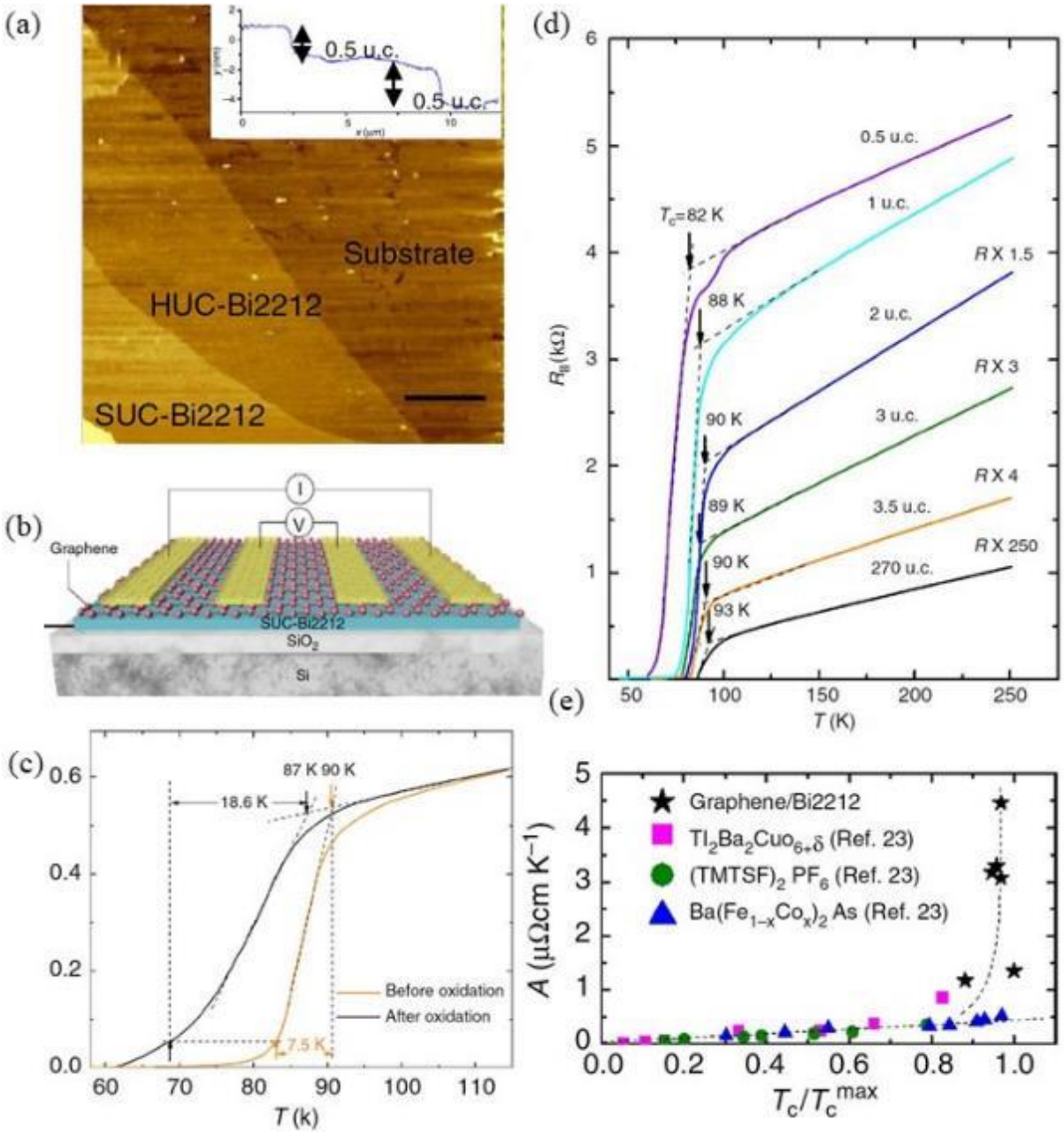

Figure 12. (a) Atomic force microscope image of a Bi2212 flake with terrace-like edges. The heights are ~2.7 nm for the lower layer and ~2.3 nm for the upper layer. (b) Schematic illustration of graphene/Bi2212 heterostructure on a SiO_2/Si substrate. (c) Normalized *R*–*T* curves for a graphene/TUC-Bi2212 heterostructure sample before and after oxidation of graphene. (d) *R*–*T* curves for Bi2212 with various thicknesses from 270-unit-cell thick to half-unit-cell thick. (e) *A* versus T_c/T_c^{max}. *A* is the slope for linear temperature-dependent resistivity in the normal state. T_c^{max} is the largest T_c among heterostructures with various thicknesses.[50]

Ultrathin Bi-2212 crystals prepared by various methods have shown diverse properties from insulating to superconducting, which makes it hard to determine the superconducting mechanism of ultrathin Bi2212.[60-62] Single-layer graphene was used as a protection layer on top of Bi2212 ultrathin flake to fabricate graphene/Bi2212 van der Waals heterostructure (Figure **12**. (a) Atomic force microscope image of a Bi2212 flake with terrace-like edges. The heights are ~2.7 nm for the lower layer and ~2.3 nm for the upper layer. (b) Schematic illustration of graphene/Bi2212 heterostructure on a SiO_2/Si substrate. (c) Normalized *R*–*T* curves for a graphene/TUC-Bi2212 heterostructure sample before and after oxidation of graphene. (d) *R*–*T* curves for Bi2212 with various thicknesses from 270-unit-cell thick to half-unit-cell thick. (e) *A* versus T_c/T_c^{max}. *A* is the slope for linear temperature-dependent resistivity in the normal state. T_c^{max} is the largest T_c among heterostructures with various thicknesses.[50]

12 a-b), realizing that superconductivity was steadily preserved for flakes with various thicknesses from 270-unit-cell down to half-unit-cell.[50] For heterostructure fabrication, thermal treatment in O_2/Ar at 200 °C was a crucial step to get intimate contact between graphene and Bi-2212. Graphene was also converted into graphene oxide to check the role of graphene in the heterostructure. For Bi2212 with a thickness of single-unit-cell (SUC) and two-unit-cell (TUC), their heterostructures both show superconducting before oxidation. By using graphene oxide, TUC-Bi2212 still kept superconducting while SUC-Bi2212 lost superconductivity. In addition, graphene oxide causes reduced transition temperature (T_c) and more than doubled transition width for TUC-Bi2212, shown in Figure **12**. (a) Atomic force microscope image of a Bi2212 flake with terrace-like edges. The heights are ~2.7 nm for the lower layer and ~2.3 nm for the upper layer. (b) Schematic illustration of graphene/Bi2212 heterostructure on a SiO_2/Si substrate. (c) Normalized *R*–*T* curves for a graphene/TUC-Bi2212 heterostructure sample before and after oxidation of graphene. (d) *R*–*T* curves for Bi2212 with various thicknesses from 270-unit-cell thick to half-unit-cell thick. (e) *A* versus T_c/T_c^{max}. *A* is the slope for linear temperature-dependent resistivity in the normal state. T_c^{max} is the largest T_c among heterostructures with various thicknesses.[50]

12c. When it comes to the effect of flake thickness on superconductivity (Figure **12**. (a) Atomic force microscope image of a Bi2212 flake with terrace-like edges. The heights are ~2.7 nm for the lower layer and ~2.3 nm for the upper layer. (b) Schematic illustration of graphene/Bi2212 heterostructure on a SiO_2/Si substrate. (c) Normalized *R*–*T* curves for a graphene/TUC-Bi2212 heterostructure sample before and after oxidation of graphene. (d) *R*–*T* curves for Bi2212 with various thicknesses from 270-unit-cell thick to half-unit-cell thick. (e) *A* versus T_c/T_c^{max}. *A* is the slope for linear temperature-dependent resistivity in the normal state. T_c^{max} is the largest T_c among heterostructures with various thicknesses.[50]

12d), T_c gradually decreases from 93 K for 270-unit-cell to 82 K for half-unit-cell. The sheet resistances at the normal state increase proportional with higher temperature, while decrease several orders of magnitude with reducing flake thickness. Furthermore, the slope of linear resistances (A) that reflects the strength of scattering shows considerable changes by a factor of 4-5 with relatively stable T_c, as seen in Figure **12**. (a) Atomic force microscope image of a Bi2212 flake with terrace-like edges. The heights are ~2.7 nm for the lower layer and ~2.3 nm for the upper layer. (b) Schematic illustration of graphene/Bi2212 heterostructure on a SiO_2/Si substrate. (c) Normalized *R*–*T* curves for a graphene/TUC-Bi2212 heterostructure sample before and after oxidation of graphene. (d) *R*–*T* curves for Bi2212 with various

thicknesses from 270-unit-cell thick to half-unit-cell thick. (e) *A* versus T_c/T_c^{max}. *A* is the slope for linear temperature-dependent resistivity in the normal state. T_c^{max} is the largest T_c among heterostructures with various thicknesses.[50]

12e. This non-linear A-T_c relationship is quite contradicted to previous reports, revealing the normal state behavior for graphene/Bi2212 heterostructure is decoupled from superconductivity. It raises a significant question for future research on the connection of large-angle scattering process with superconductivity.

6. Summary and perspective

We briefly reviewed the recent discovered atomically thin superconducting material systems, including elemental superconductors, FeSe and cuprate superconductors. These studies clearly indicate that the interface is the key to high-temperature superconductivity in atomically thin iron-based and cuprate superconductors. The interface superconductivity enhancement effect in atomically thin superconductors has now been proved as a unique method for discovering new high-temperature superconductors and a possible tool to unveil the fascinating high-temperature superconductivity mechanism. Studies on atomically thin superconductors are focused by many top research groups working on superconducting materials worldwide. It is highly possible that the next breakthrough in superconductors will come soon.

Acknowledgments

The authors acknowledge support from the Australian Research Council (ARC) through the ARC Centre of Excellence in Future Low-Energy Electronics Technologies (FLEET, CE170100039). X.L.W. acknowledges support from the Australian Research Council (ARC) through an ARC Discovery Project (DP130102956) and an ARC Professorial Future Fellowship project (FT130100778). Z. Li acknowledges support from the ARC through DP160101474, DP170104116 and DE190100219.

Keywords

Atomically thin, interface, iron-based superconductors, cuprate superconductors, high-temperature

Reference

[1] H. K. Onnes, *Comm. Leiden* **1911**, 122, 2.
[2] J. Bardeen, L. N. Cooper, J. R. Schrieffer, *Physical review* **1957**, 108, 1175.
[3] J. de Launay, *Physical Review* **1954**, 93, 661.
[4] J. G. Bednorz, K. A. Müller, *Zeitschrift für Physik B Condensed Matter* **1986**, 64, 189-193.
[5] M.-K. Wu, J. R. Ashburn, C. Torng, P. H. Hor, R. L. Meng, L. Gao, Z. J. Huang, Y. Wang, a. Chu, *Physical review letters* **1987**, 58, 908.
[6] Y. Kamihara, T. Watanabe, M. Hirano, H. Hosono, *Journal of the American Chemical Society* **2008**, 130, 3296-3297.
[7] Z.-A. Ren, W. Lu, J. Yang, W. Yi, X.-L. Shen, Z.-C. Li, G.-C. Che, X.-L. Dong, L.-L. Sun, F. Zhou, *arXiv preprint arXiv:0804.2053* **2008**.
[8] C. Wang, L. Li, S. Chi, Z. Zhu, Z. Ren, Y. Li, Y. Wang, X. Lin, Y. Luo, S. Jiang, *EPL (Europhysics Letters)* **2008**, 83, 67006.
[9] V. Ginzburg, *Phys. Letters* **1964**, 13.
[10] J. Pereiro, A. Petrovic, C. Panagopoulos, I. Božović, *arXiv preprint arXiv:1111.4194* **2011**.
[11] S. Gariglio, M. Gabay, J. Mannhart, J.-M. Triscone, *Physica C: Superconductivity and its Applications* **2015**, 514, 189-198.
[12] W. Qing-Yan, L. Zhi, Z. Wen-Hao, Z. Zuo-Cheng, Z. Jin-Song, L. Wei, D. Hao, O. Yun-Bo, D. Peng, C. Kai, *Chinese Physics Letters* **2012**, 29, 037402.
[13] L. Wang, X. Ma, Q.-K. Xue, *Superconductor Science and Technology* **2016**, 29, 123001.
[14] Z. Wang, C. Liu, Y. Liu, J. Wang, *Journal of Physics: Condensed Matter* **2017**, 29, 153001.
[15] T. Uchihashi, *Superconductor Science and Technology* **2016**, 30, 013002.
[16] T. Zhang, P. Cheng, W.-J. Li, Y.-J. Sun, G. Wang, X.-G. Zhu, K. He, L. Wang, X. Ma, X. Chen, *Nature Physics* **2010**, 6, 104.
[17] H.-M. Zhang, Y. Sun, W. Li, J.-P. Peng, C.-L. Song, Y. Xing, Q. Zhang, J. Guan, Z. Li, Y. Zhao, *Physical review letters* **2015**, 114, 107003.
[18] F.-C. Hsu, J.-Y. Luo, K.-W. Yeh, T.-K. Chen, T.-W. Huang, P. M. Wu, Y.-C. Lee, Y.-L. Huang, Y.-Y. Chu, D.-C. Yan, *Proceedings of the National Academy of Sciences* **2008**, 105, 14262-14264.
[19] S. Medvedev, T. McQueen, I. Troyan, T. Palasyuk, M. Eremets, R. J. Cava, S. Naghavi, F. Casper, V. Ksenofontov, G. Wortmann, *Nature materials* **2009**, 8, 630.
[20] C.-L. Song, Y.-L. Wang, P. Cheng, Y.-P. Jiang, W. Li, T. Zhang, Z. Li, K. He, L. Wang, J.-F. Jia, *Science* **2011**, 332, 1410-1413.
[21] C.-L. Song, Y.-L. Wang, Y.-P. Jiang, Z. Li, L. Wang, K. He, X. Chen, X.-C. Ma, Q.-K. Xue, *Physical Review B* **2011**, 84, 020503.
[22] Z. Wen-Hao, S. Yi, Z. Jin-Song, L. Fang-Sen, G. Ming-Hua, Z. Yan-Fei, Z. Hui-Min, P. Jun-Ping, X. Ying, W. Hui-Chao, *Chinese Physics Letters* **2014**, 31, 017401.
[23] L. Deng, B. Lv, Z. Wu, Y. Xue, W. Zhang, F. Li, L. Wang, X. Ma, Q. Xue, C. Chu, *Physical Review B* **2014**, 90, 214513.
[24] Y. Sun, W. Zhang, Y. Xing, F. Li, Y. Zhao, Z. Xia, L. Wang, X. Ma, Q.-K. Xue, J. Wang, *Scientific reports* **2014**, 4, 6040.

[25] Z. Zhang, Y.-H. Wang, Q. Song, C. Liu, R. Peng, K. Moler, D. Feng, Y. Wang, *Science bulletin* **2015**, 60, 1301-1304.
[26] J.-F. Ge, Z.-L. Liu, C. Liu, C.-L. Gao, D. Qian, Q.-K. Xue, Y. Liu, J.-F. Jia, *Nature materials* **2015**, 14, 285.
[27] W. Zhang, Z. Li, F. Li, H. Zhang, J. Peng, C. Tang, Q. Wang, K. He, X. Chen, L. Wang, *Physical Review B* **2014**, 89, 060506.
[28] Z. Li, J.-P. Peng, H.-M. Zhang, W.-H. Zhang, H. Ding, P. Deng, K. Chang, C.-L. Song, S.-H. Ji, L. Wang, *Journal of Physics: Condensed Matter* **2014**, 26, 265002.
[29] S. He, J. He, W. Zhang, L. Zhao, D. Liu, X. Liu, D. Mou, Y.-B. Ou, Q.-Y. Wang, Z. Li, *Nature materials* **2013**, 12, 605.
[30] S. Tan, Y. Zhang, M. Xia, Z. Ye, F. Chen, X. Xie, R. Peng, D. Xu, Q. Fan, H. Xu, *Nature materials* **2013**, 12, 634.
[31] J. Lee, F. Schmitt, R. Moore, S. Johnston, Y.-T. Cui, W. Li, M. Yi, Z. Liu, M. Hashimoto, Y. Zhang, *Nature* **2014**, 515, 245.
[32] Q. Fan, W. Zhang, X. Liu, Y. Yan, M. Ren, R. Peng, H. Xu, B. Xie, J. Hu, T. Zhang, *Nature Physics* **2015**, 11, 946.
[33] Q. Wang, W. Zhang, Z. Zhang, Y. Sun, Y. Xing, Y. Wang, L. Wang, X. Ma, Q.-K. Xue, J. Wang, *2D Materials* **2015**, 2, 044012.
[34] H. Ding, Y.-F. Lv, K. Zhao, W.-L. Wang, L. Wang, C.-L. Song, X. Chen, X.-C. Ma, Q.-K. Xue, *Physical review letters* **2016**, 117, 067001.
[35] C.-L. Song, H.-M. Zhang, Y. Zhong, X.-P. Hu, S.-H. Ji, L. Wang, K. He, X.-C. Ma, Q.-K. Xue, *Physical review letters* **2016**, 116, 157001.
[36] Y. Wang, H. Sun, S. Tan, H. Feng, Z. Cheng, J. Zhao, A. Zhao, B. Wang, Y. Luo, J. Yang, *Nature communications* **2013**, 4, 2214.
[37] G. Zhou, Q. Zhang, F. Zheng, D. Zhang, C. Liu, X. Wang, C.-L. Song, K. He, X.-C. Ma, L. Gu, *Science bulletin* **2018**, 63, 747-752.
[38] F. Li, Q. Zhang, C. Tang, C. Liu, J. Shi, C. Nie, G. Zhou, Z. Li, W. Zhang, C.-L. Song, *2D Materials* **2016**, 3, 024002.
[39] C. Colliex, T. Manoubi, C. Ortiz, *Physical Review B* **1991**, 44, 11402.
[40] J. Y. T. Wei, C. C. Tsuei, P. J. M. van Bentum, Q. Xiong, C. W. Chu, M. K. Wu, *Physical Review B* **1998**, 57, 3650-3662.
[41] J. G. Bednorz, K. A. Müller, *Zeitschrift für Physik B Condensed Matter* **1986**, 64, 189-193.
[42] M. K. Wu, J. R. Ashburn, C. J. Torng, P. H. Hor, R. L. Meng, L. Gao, Z. J. Huang, Y. Q. Wang, C. W. Chu, *Physical Review Letters* **1987**, 58, 908-910.
[43] A. Schilling, M. Cantoni, J. D. Guo, H. R. Ott, *Nature* **1993**, 363, 56-58.
[44] K. Yamada, K. Kurahashi, T. Uefuji, M. Fujita, S. Park, S. H. Lee, Y. Endoh, *Physical Review Letters* **2003**, 90, 137004.
[45] C. Bernhard, J. L. Tallon, T. Blasius, A. Golnik, C. Niedermayer, *Physical Review Letters* **2001**, 86, 1614-1617.
[46] H.-H. Wen, L. Shan, X.-G. Wen, Y. Wang, H. Gao, Z.-Y. Liu, F. Zhou, J. Xiong, W. Ti, *Physical Review B* **2005**, 72, 134507.
[47] K. Fujita, A. R. Schmidt, E.-A. Kim, M. J. Lawler, D. Hai Lee, J. C. Davis, H. Eisaki, S.-i. Uchida, *Journal of the Physical Society of Japan* **2011**, 81, 011005.
[48] M. Hashimoto, T. Yoshida, K. Tanaka, A. Fujimori, M. Okusawa, S. Wakimoto, K. Yamada, T. Kakeshita, H. Eisaki, S. Uchida, *Physical Review B* **2007**, 75, 140503.
[49] D. Feng, A. Damascelli, K. Shen, N. Motoyama, D. Lu, H. Eisaki, K. Shimizu, J.-i. Shimoyama, K. Kishio, N. Kaneko, *Physical review letters* **2002**, 88, 107001.
[50] D. Jiang, T. Hu, L. You, Q. Li, A. Li, H. Wang, G. Mu, Z. Chen, H. Zhang, G. Yu, J. Zhu, Q. Sun, C. Lin, H. Xiao, X. Xie, M. Jiang, *Nature Communications* **2014**, 5, 5708.

[51] Ø. Fischer, M. Kugler, I. Maggio-Aprile, C. Berthod, C. Renner, *Reviews of Modern Physics* **2007**, 79, 353-419.
[52] M. Hashimoto, I. M. Vishik, R.-H. He, T. P. Devereaux, Z.-X. Shen, *Nature Physics* **2014**, 10, 483.
[53] J. A. Slezak, J. Lee, M. Wang, K. McElroy, K. Fujita, B. M. Andersen, P. J. Hirschfeld, H. Eisaki, S. Uchida, J. C. Davis, *Proceedings of the National Academy of Sciences* **2008**, 105, 3203.
[54] Y.-F. Lv, W.-L. Wang, J.-P. Peng, H. Ding, Y. Wang, L. Wang, K. He, S.-H. Ji, R. Zhong, J. Schneeloch, G.-D. Gu, C.-L. Song, X.-C. Ma, Q.-K. Xue, *Physical Review Letters* **2015**, 115, 237002.
[55] Y. Zhong, Y. Wang, S. Han, Y.-F. Lv, W.-L. Wang, D. Zhang, H. Ding, Y.-M. Zhang, L. Wang, K. He, R. Zhong, J. A. Schneeloch, G.-D. Gu, C.-L. Song, X.-C. Ma, Q.-K. Xue, *Science Bulletin* **2016**, 61, 1239-1247.
[56] K. Jiang, X. Wu, J. Hu, Z. Wang, *Physical Review Letters* **2018**, 121, 227002.
[57] G.-Y. Zhu, F.-C. Zhang, G.-M. Zhang, *Physical Review B* **2016**, 94, 174501.
[58] Y. Zhong, S. Han, Y. Wang, Z. Luo, D. Zhang, L. Wang, W. Li, K. He, C.-L. Song, X.-C. Ma, Q.-K. Xue, *Physical Review B* **2018**, 97, 245420.
[59] M. Liao, Y. Zhu, J. Zhang, R. Zhong, J. Schneeloch, G. Gu, K. Jiang, D. Zhang, X. Ma, Q.-K. Xue, *Nano Letters* **2018**, 18, 5660-5665.
[60] K. Saito, M. Kaise, *Physical Review B* **1998**, 57, 11786-11791.
[61] L. X. You, A. Yurgens, D. Winkler, C. T. Lin, B. Liang, *Superconductor Science and Technology* **2006**, 19, S205-S208.
[62] I. Bozovic, G. Logvenov, I. Belca, B. Narimbetov, I. Sveklo, *Physical review letters* **2002**, 89, 107001.